

# Statistical nature of non-Gaussianity from cubic order primordial perturbations: CMB map simulations and genus statistic

Pravabati Chingangbam and Changbom Park

E-mail: prava@kias.re.kr, cbp@kias.re.kr  
Korea Institute for Advanced Study, Hoegiro 87, Dongdaemun-gu, Seoul 130722,  
South Korea.

**Abstract.** We simulate CMB maps including non-Gaussianity arising from cubic order perturbations of the primordial gravitational potential, characterized by the non-linearity parameter  $g_{\text{NL}}$ . The maps are used to study the characteristic nature of the resulting non-Gaussian temperature fluctuations. We measure the genus and investigate how it deviates from Gaussian shape as a function of  $g_{\text{NL}}$  and smoothing scale. We find that the deviation of the non-Gaussian genus curve from the Gaussian one has an antisymmetric, sine function like shape, implying more hot and more cold spots for  $g_{\text{NL}} > 0$  and less of both for  $g_{\text{NL}} < 0$ . The deviation increases linearly with  $g_{\text{NL}}$  and also exhibits mild increase as the smoothing scale increases. We further study other statistics derived from the genus, namely, the number of hot spots, the number of cold spots, combined number of hot and cold spots and the slope of the genus curve at mean temperature fluctuation. We find that these observables carry signatures of  $g_{\text{NL}}$  that are clearly distinct from the quadratic order perturbations, encoded in the parameter  $f_{\text{NL}}$ . Hence they can be very useful tools for distinguishing not only between non-Gaussian temperature fluctuations and Gaussian ones but also between  $g_{\text{NL}}$  and  $f_{\text{NL}}$  type non-Gaussianities.

## 1. Introduction

Since the discovery of the temperature anisotropies of the cosmic microwave background radiation [1] their statistical nature has been subject of intense study. If inflation [2, 3, 4], as strongly supported by observations, is indeed the mechanism that gave rise to these anisotropies, then their statistical nature must be inherited from those of the primordial density fluctuations. All models of inflation, in general, predict some amount of deviation of these fluctuations from a Gaussian distribution. The detailed knowledge of the deviations are quite model dependent. This makes it a good discriminant between various models of inflation. The observational search for non-Gaussianity is, however, beset with serious difficulties since various spurious observational effects can mask the true signal.

Primordial non-Gaussianity arises from higher order terms in the perturbative expansion of the primordial gravitational potential,  $\Phi$ , which must be taken into account in the presence of higher order interaction. In this paper, we consider the following expansion of the *local* type [5, 6, 7]:

$$\Phi(\mathbf{x}) = \Phi^L(\mathbf{x}) + f_{\text{NL}} ((\Phi^L(\mathbf{x}))^2 - \langle (\Phi^L)^2 \rangle) + g_{\text{NL}} (\Phi^L(\mathbf{x}))^3 + \dots, \quad (1)$$

where  $f_{\text{NL}}$  and  $g_{\text{NL}}$  are parameters that measure the level of non-linearity and  $\Phi^L$  is the linear order perturbation. This expansion is rather special in that it assumes that the higher order perturbations are known in terms of the linear field, with our ignorance pushed into  $f_{\text{NL}}$  and  $g_{\text{NL}}$ . Also, they depend only on the linear field value at the same spatial point. Such an expansion is not a generic prediction of all inflation models. In general, it can be a much more complicated expression involving convolutions of the products of  $\Phi^L$ 's (*non-local*) with the non-linearity parameters being scale dependent kernels. Generally, the predictions of inflation are quantified by  $n$ -point functions in Fourier space. Eq.(1) holds provided the  $n$ -point functions have most of the signal coming from some special configurations of the wave vectors. For the 3-point function, this corresponds to having the amplitude of one of the wave vectors tending to zero, the so called *squeezed* configuration. For the 4-point function, it corresponds to either one of the wave vectors tending to zero or two of them tending to zero [8, 9, 10, 11]. Here we ignore any possible scale dependence of  $f_{\text{NL}}$  and  $g_{\text{NL}}$  to simplify the problem. This is justified by current experimental limitations. The bulk of the study on the topic, both theoretical and observational, has been focused primarily on the quadratic order non-Gaussianity [6, 12, 13, 14, 15, 16]. The strongest limits on  $f_{\text{NL}}$  from CMB observations obtained so far is  $-4 < f_{\text{NL}} < 80$  (at 95% CL) [17].

There is now growing interest in the cubic order perturbation and its observability. The question is whether the cubic term is negligible, comparable or even dominant when compared to the quadratic term. For the standard single field and uncoupled multiple fields slow-roll inflation they are found to be slow roll suppressed and hence negligibly small [9, 18]. (See [19] for attempt to get large trispectrum in single field inflation). However, in the curvaton scenario [20, 21] it can happen that the cubic term is comparable or even dominant to the quadratic term [22, 23, 24, 25, 26, 27]. Another class

of models with similar predictions is the so called multibrid inflation [28, 29, 30]. Thus, the possibility arises that the dominant source for primordial non-Gaussianity comes from the cubic non-linearity and it becomes important to understand theoretically how observational quantities in the CMB as well as the large scale structure get affected by it. Early studies of the consequences on the CMB have focused on the angular trispectrum of the temperature fluctuations [5, 31, 32], while feasibility study of measurement of the trispectrum from observational data was performed in [33]. Implications of  $g_{\text{NL}}$  on galaxy bispectrum was studied in [34]. The first limit on  $g_{\text{NL}}$  using SDSS data and N-body simulations has been obtained to be  $-3.5 \times 10^5 < g_{\text{NL}} < +8.2 \times 10^5$  (at 95% CL) in [35]. No bounds have been obtained using CMB data as yet.

An important step towards understanding how the primordial non-Gaussianities affect the CMB temperature fluctuations is to simulate maps with the non-Gaussianities going in as input in the map making process. Since we have control over the input parameters, namely,  $f_{\text{NL}}$  and  $g_{\text{NL}}$  in this case, we can test and calibrate the sensitivities of different statistical observables to these parameters, using the simulated maps. Observational contaminants can be added to find out exactly how each one of them can mask the real non-Gaussian effects and experimental bounds can be obtained for the input parameters by comparing with observational data. There are several map making methods that have been proposed in the literature for  $f_{\text{NL}}$  non-Gaussianity. Komatsu *et al.* [36] used a straightforward method of generating a Gaussian random realization of the linear gravitational potential in Fourier space and then convolving two such fields to obtain the quadratic term in Eq.(10). Liguori *et al.* [37] proposed a fast algorithm which require the computation to be done in real space rather than Fourier space. Other methods involve the input of given power spectrum, bispectrum and higher order spectra [38, 39], or some known correlation structure of the non-Gaussian field [40], or using spherical wavelets [41].

Simulated non-Gaussian CMB maps arising from  $g_{\text{NL}}$  term have not been discussed in the literature as yet and we present them in this paper. The goal is to study how the cubic perturbations show up as non-Gaussianity of the temperature anisotropies. We use the genus, which is the number of isolated hot spots minus the number of isolated cold spots, as our statistical observable. We first make simulations of non-Gaussian maps with  $g_{\text{NL}}$  as the input parameter, extending the method of [37] and using the full linear radiation transfer function. In order to be able to investigate the pure effects of the  $g_{\text{NL}}$  term we have set  $f_{\text{NL}} = 0$  in our simulations. Then, we use these maps to compute the genus statistic to find out how it varies as a function of  $g_{\text{NL}}$  and the smoothing scale. Further, we discuss four new statistics derived from the genus and show that they can be very useful tools to distinguish primordial non-Gaussianity from Gaussianity and also to distinguish between  $f_{\text{NL}}$  and  $g_{\text{NL}}$  type non-Gaussianities.

This paper is organized as follows: in section 2 we outline the method for generating the non-Gaussian maps, describe the implementation of the map making process and we present our results of the non-Gaussian maps and the one-point PDF. In section 3 we compute the genus using the simulated maps and show how they deviate from

the Gaussian shape. We then discuss the derived statistics and elaborate on their characteristics and how they distinguish  $g_{\text{NL}}$  from  $f_{\text{NL}}$ . We conclude with a summary of results and remarks on direction for future work in Section 4.

## 2. Simulation of non-Gaussian maps

We briefly review the method for simulating non-Gaussian maps outlined in [37] with a simple extension to include  $g_{\text{NL}}$  term.

### 2.1. Calculating $a_{\ell m}$ 's in real space

The CMB temperature fluctuations are usually expanded in terms of spherical harmonics as  $\Delta T(\hat{n}) = \sum_{\ell m} a_{\ell m} Y_{\ell m}(\hat{n})$ . The  $a_{\ell m}$ 's are then computed by convolving the primordial potential fluctuations with the radiation transfer function  $\Delta_\ell(r)$  as,

$$a_{\ell m} = 4\pi(-i)^\ell \int \frac{d^3 k}{(2\pi)^3} \Phi(\mathbf{k}) \Delta_\ell(k) Y_{\ell m}^*(\hat{\mathbf{k}}), \quad (2)$$

where  $\Phi(\mathbf{k})$  is the Fourier transform of the real space potential  $\Phi(\mathbf{x})$ .  $\Delta_\ell(k)$  encodes the evolution history of the CMB photons in their journey from recombination till now. Defining

$$\Phi_{\ell m}(k) \equiv \int d\Omega_{\hat{k}} \Phi(\mathbf{k}) Y_{\ell m}(\hat{k}). \quad (3)$$

we can rewrite  $a_{\ell m}$  as

$$a_{\ell m} = \frac{(-i)^\ell}{2\pi^2} \int dk k^2 \Phi_{\ell m}(k) \Delta_\ell(k), \quad (4)$$

To rewrite Eq. (4) as an integral in real space, define the real space harmonic potential

$$\Phi_{\ell m}(r) \equiv \frac{(-i)^\ell}{2\pi^2} \int dk k^2 \Phi_{\ell m}(k) j_\ell(kr), \quad (5)$$

and its inverse

$$\Phi_{\ell m}(k) = 4\pi(i)^\ell \int dr r^2 \Phi_{\ell m}(r) j_\ell(kr), \quad (6)$$

where  $j_\ell$ 's are spherical Bessel functions. Then, insert Eqn. (6) in (4) and define

$$\Delta_\ell(r) \equiv \frac{2}{\pi} \int dk k^2 \Delta_\ell(k) j_\ell(kr), \quad (7)$$

we can then write:

$$a_{\ell m} = \int dr r^2 \Phi_{\ell m}(r) \Delta_\ell(r). \quad (8)$$

For non-Gaussian  $\Phi$  given by Eq.(10), we would have

$$\Phi(\mathbf{k}) = \Phi^{\text{L}}(\mathbf{k}) + f_{\text{NL}} \Phi^{\text{NL}}(\mathbf{k}) + g_{\text{NL}} \Phi^{\text{NNL}}(\mathbf{k}), \quad (9)$$

where

$$\begin{aligned}\Phi^{\text{NL}}(\mathbf{k}) &= \int \frac{d^3k_1}{(2\pi)^3} \Phi^{\text{L}}(\mathbf{k} + \mathbf{k}_1) \Phi^{\text{L}}(\mathbf{k}_1), \\ \Phi^{\text{NNL}}(\mathbf{k}) &= \int \frac{d^3k_1}{(2\pi)^3} \frac{d^3k_2}{(2\pi)^3} \Phi^{\text{L}}(\mathbf{k} + \mathbf{k}_1 + \mathbf{k}_2) \Phi^{\text{L}}(\mathbf{k}_1) \Phi^{\text{L}}(\mathbf{k}_2).\end{aligned}\quad (10)$$

We can then define harmonic components  $\Phi_{\ell m}^{\text{NL}}$  and  $\Phi_{\ell m}^{\text{NNL}}$  in Fourier and real space using Eqs. (5) and (6), to give us

$$\Phi_{\ell m}(k) \equiv \Phi_{\ell m}^{\text{L}}(k) + f_{\text{NL}} \Phi_{\ell m}^{\text{NL}}(k) + g_{\text{NL}} \Phi_{\ell m}^{\text{NNL}}(k).\quad (11)$$

$a_{\ell m}$  is then given by

$$a_{\ell m} = a_{\ell m}^{\text{L}} + f_{\text{NL}} a_{\ell m}^{\text{NL}} + g_{\text{NL}} a_{\ell m}^{\text{NNL}},\quad (12)$$

where each term is an integral over the corresponding  $\Phi$ .

Thus, we need to compute four quantities, namely,  $\Delta_\ell(r)$ ,  $\Phi_{\ell m}^{\text{L}}(r)$ ,  $\Phi_{\ell m}^{\text{NL}}(r)$  and  $\Phi_{\ell m}^{\text{NNL}}(r)$ , in order to get  $a_{\ell m}$  upto cubic order primordial perturbations.  $\Delta_\ell(r)$  can be independently computed using  $\Delta_\ell(k)$  obtained from CMBFAST [42]. In order to generate  $\Phi_{\ell m}^{\text{L}}(r)$  we need its correlation function given by [37],

$$\langle \Phi_{\ell_1 m_1}^{\text{L}}(r_1) \Phi_{\ell_2 m_2}^{\text{L}*}(r_2) \rangle = \frac{2}{\pi} \delta_{\ell_1}^{\ell_2} \delta_{m_1}^{m_2} \int dk k^2 P_\Phi(k) j_{\ell_1}(kr_1) j_{\ell_2}(kr_2),\quad (13)$$

where  $P_\Phi(k)$  is the primordial power spectrum (for the Gaussian part of  $\Phi$ ), given by

$$P_\Phi(k) = \frac{A_0}{k^3} \left( \frac{k}{k_0} \right)^{n_s - 1},\quad (14)$$

with  $A_0$  being the amplitude,  $k_0$  is some suitable pivot scale and  $n_s$  is the spectral index. Then,  $\Phi_{\ell m}^{\text{L}}(r)$  can be obtained from the integral

$$\Phi_{\ell m}^{\text{L}}(r) = \int dr_1 r_1^2 n_{\ell m}(r_1) W_\ell(r, r_1),\quad (15)$$

where  $n_{\ell m}(r)$  are independent complex Gaussian variables characterized by the correlation function

$$\langle n_{\ell_1 m_1}(r_1) n_{\ell_2 m_2}^*(r_2) \rangle = \frac{\delta^D(r_1 - r_2)}{r^2} \delta_{\ell_1}^{\ell_2} \delta_{m_1}^{m_2};\quad (16)$$

and  $W_\ell(r, r_1)$  are filter functions defined as

$$W_\ell(r, r_1) = \frac{2}{\pi} \int dk k^2 \sqrt{P_\Phi(k)} j_\ell(kr) j_\ell(kr_1).\quad (17)$$

For fixed  $r$ ,  $W_\ell(r, r_1)$  is a smooth function of  $r_1$  and sharply peaked at  $r = r_1$ . Simplified expressions which are convenient for numerical calculation of  $W_\ell(r, r_1)$  are given in Appendix A.

To compute  $\Phi_{\ell m}^{\text{NL}}$ , first compute the linear potential  $\Phi^{\text{L}}(\mathbf{r}) = \sum_{\ell m} \Phi_{\ell m}^{\text{L}}(r) Y_{\ell m}(\hat{r})$  and square it to obtain  $\Phi^{\text{NL}}(\mathbf{r})$ . Then harmonic transform to get  $\Phi_{\ell m}^{\text{NL}}(r)$ . Similarly,  $\Phi_{\ell m}^{\text{NNL}}$ , can be computed by first taking cube of  $\Phi^{\text{L}}(\mathbf{r})$  to obtain  $\Phi^{\text{NNL}}(\mathbf{r})$  and then harmonic transforming to get  $\Phi_{\ell m}^{\text{NNL}}(r)$ . Finally, putting  $f_{\text{NL}} = 0$  we get,

$$\Delta T = \Delta T^{\text{G}} + g_{\text{NL}} \Delta T^{\text{NG}}.\quad (18)$$

This method is particularly useful for calculating the  $g_{\text{NL}}$  case because had we done the calculation in  $k$  space we would have had to convolve three  $\Phi^{\text{L}}$ 's as in Eqn.(10).

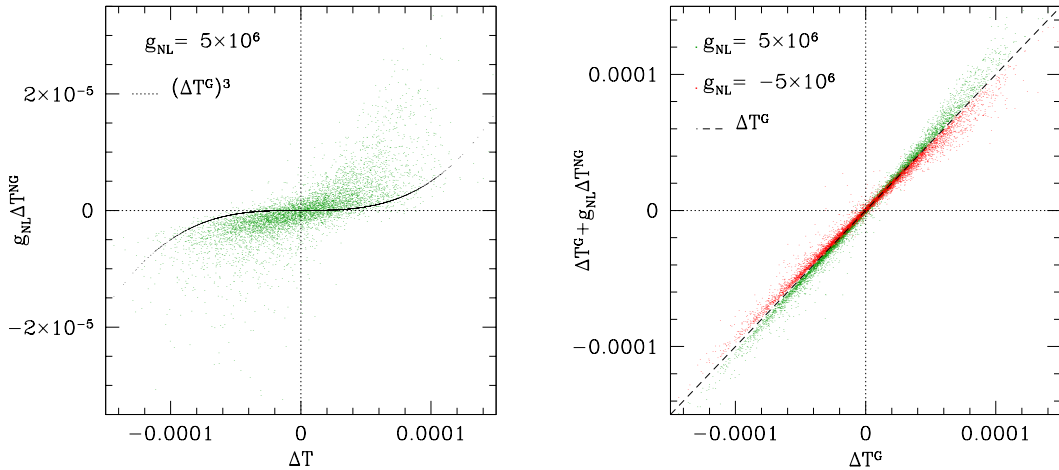


**Figure 1.** Pixel Distribution of  $\Delta T^{\text{NG}}$  with respect to  $\Delta T^{\text{G}}$ .

## 2.2. Implementation of the algorithm

We use a  $\Lambda$ CDM cosmological model with primordial spectral index  $n_s = 1$ . We have used the WMAP 5 year parameters [43] given by  $\Omega_c = 0.233$ ,  $\Omega_b = 0.0462$ ,  $\Omega_\Lambda = 0.721$ ,  $\tau_{re} = 0.087$ ,  $h_0 = 0.719$ . With these parameters, the conformal time today is  $\tau_0 = 14360 \text{ Mpc}^{-1}$ . The accuracy of  $\Phi_{\ell m}^L(r)$  can be tested by computing its ‘angular power spectrum’ [44], which for  $n_s = 1$  is obtained as  $\frac{1}{2\ell+1} \sum_m |\Phi_{\ell m}^L(r)|^2 \propto 1/\ell(\ell+1)$ . We have sampled  $r$  at 472 points, with different step sizes chosen at different epochs, based on the shape of  $\Delta_\ell(r)$ . The accuracy of the resulting Gaussian  $C_\ell$  was tested by averaging over several maps and then comparing with the theoretical output of CMBFAST. We have used the Healpix package [45] to perform the harmonic transforms and the CMBFAST package [42] to compute the radiation transfer functions  $\Delta_\ell(k)$ . We have fixed  $\ell_{\text{max}} = 1100$  and the harmonic transforms have been computed using  $N_{\text{side}} = 512$ . We find that the  $g_{\text{NL}}$  term begins to dominate the linear term roughly around  $g_{\text{NL}} \sim 10^7$  and hence the perturbation expansion of  $\Phi$  is invalid beyond this value. The Gaussian maps are normalized by CMBFAST, while the non-Gaussian ones are normalized by matching the values of  $C_\ell$  at the first acoustic peak,  $\ell = 220$ , with the Gaussian one.

In Fig.(1) we show for one simulation, how for a given pixel  $g_{\text{NL}} \Delta T^{\text{NG}}$  and  $\Delta T^{\text{G}}$  are correlated. Each of the green and blue dots represents a pixel. The left panel shows the pixel distribution of pure non-Gaussian temperature  $\Delta T^{\text{NG}}$  about the  $(\Delta T^{\text{G}})^3$  curve. The right panel shows how the full  $\Delta T$ , deviates from the  $\Delta T^{\text{G}}$  line, for positive and negative values of  $g_{\text{NL}}$ .

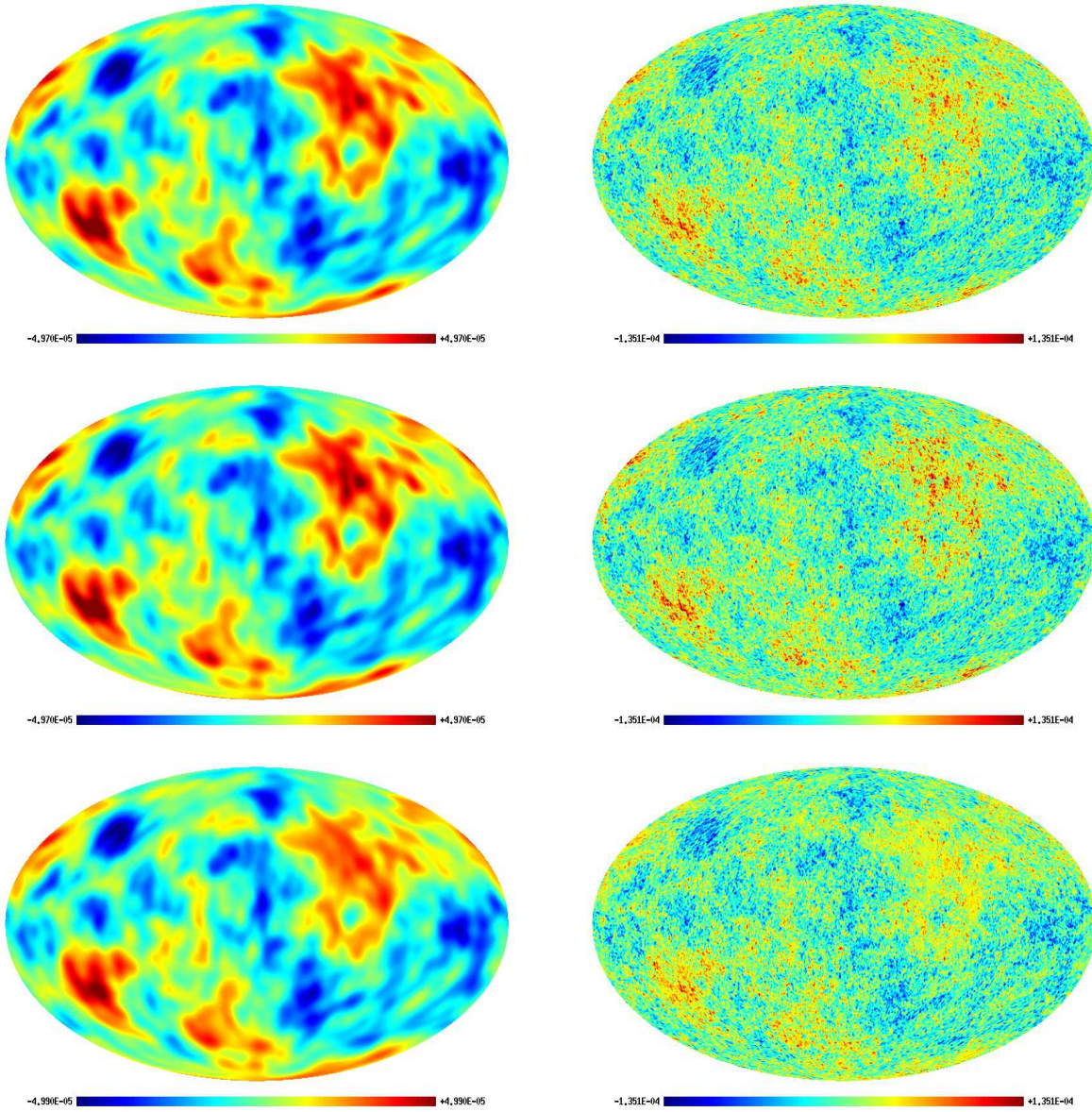


**Figure 2.** All maps in this figure are obtained from one Gaussian realization. The left-hand ones are smoothed by  $\text{FWHM} = 7^\circ$  while the right hand ones are smoothed by  $\text{FWHM} = 30'$ . The top ones are Gaussian, middle are non-Gaussian with  $g_{\text{NL}} = 5 \times 10^6$  and the bottom ones have  $g_{\text{NL}} = -5 \times 10^6$ .

### 2.3. Non-Gaussian maps and 1-point PDF

Gaussian and non-Gaussian maps obtained for the same Gaussian realization, for two different Gaussian smoothing scales, are shown in Fig. (2). The positive  $g_{\text{NL}}$  maps show hot spots that are relatively hotter than those in the Gaussian map. On the other hand, the maps with negative  $g_{\text{NL}}$  show relatively cooler hotspots. The large  $g_{\text{NL}}$  value  $\pm 5 \times 10^6$  is chosen to make the differences in the maps visible. Note that the maps vary from realization to realization due to statistical fluctuations and at such large value of  $g_{\text{NL}}$  the non-Gaussian term of the temperature fluctuation may dominate over the

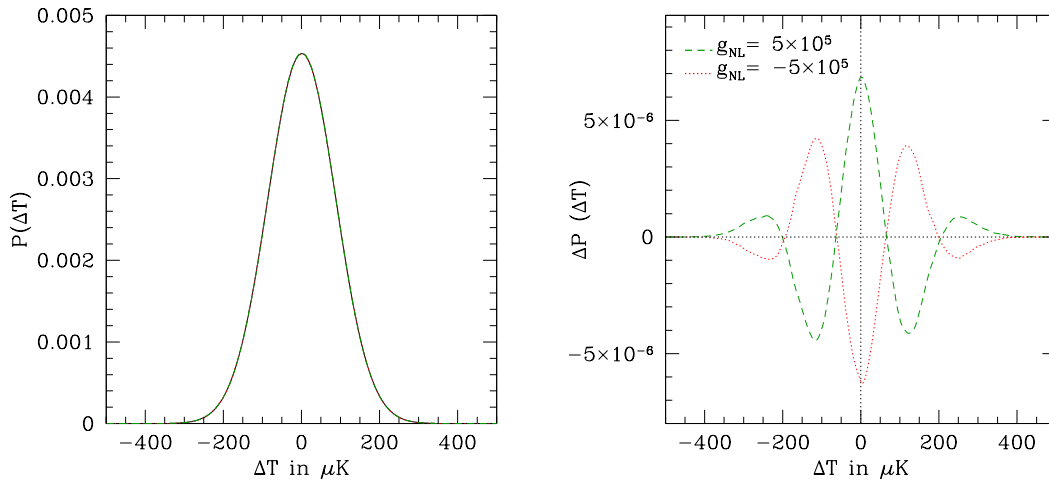


**Figure 3.** Effect of  $g_{\text{NL}}$  on 1-point PDF. Black (solid) line correspond to Gaussian, while green (dashed) corresponds to non-Gaussian with  $g_{\text{NL}} > 0$  and red (dotted) corresponds to  $g_{\text{NL}} < 0$ . Results are averaged over 150 Gaussian and non-Gaussian maps smoothed with  $\text{FWHM}=30'$ . The right panel shows the deviation of  $P(\Delta T)$  of the non-Gaussian maps from the Gaussian ones.

Gaussian part for some realizations. We have shown here a realization which is close to the average behavior indicated by the average 1-point PDF described below and for which the non-Gaussian term is still sub-dominant to the Gaussian term despite the large value of  $g_{\text{NL}}$ .

The 1-point PDF's,  $P(\Delta T)$ , are plotted in Fig. (3) for  $g_{\text{NL}} = \pm 5 \times 10^5$  and  $\text{FWHM}=30'$ , averaged over 150 realizations.  $\Delta P$  is the difference between non-Gaussian and Gaussian PDF's and we have shown them in the right hand side of Fig. (3) for positive and negative  $g_{\text{NL}}$ 's. We see that for both positive and negative  $g_{\text{NL}}$ , the mean position is not affected, as expected from the fact that non-Gaussian part comes from  $(\Phi^{\text{L}})^3$ . Positive  $g_{\text{NL}}$  increases the pixels around the mean temperature fluctuations, decreases the intermediate temperature range and again increases the hottest and coldest ranges, leading to leptokurtic shape of the 1-point PDF relative to the Gaussian one. Negative  $g_{\text{NL}}$  has the opposite effect and results in platykurtic shape of the 1-point PDF relative to the Gaussian one. These effects become more pronounced as we increase  $g_{\text{NL}}$  and corroborates what we observe visually in the maps shown in Fig. (2). On the angular power spectrum,  $C_\ell$ , both positive and negative  $g_{\text{NL}}$  increase the low scale power with negative  $g_{\text{NL}}$  having a stronger effect.

### 3. Genus statistic

By means of iso-temperature contours of the temperature fluctuation field one can study its global morphological properties. The genus, which is the number of isolated hot spots minus the number of isolated cold spots, can be obtained from the contours for a given



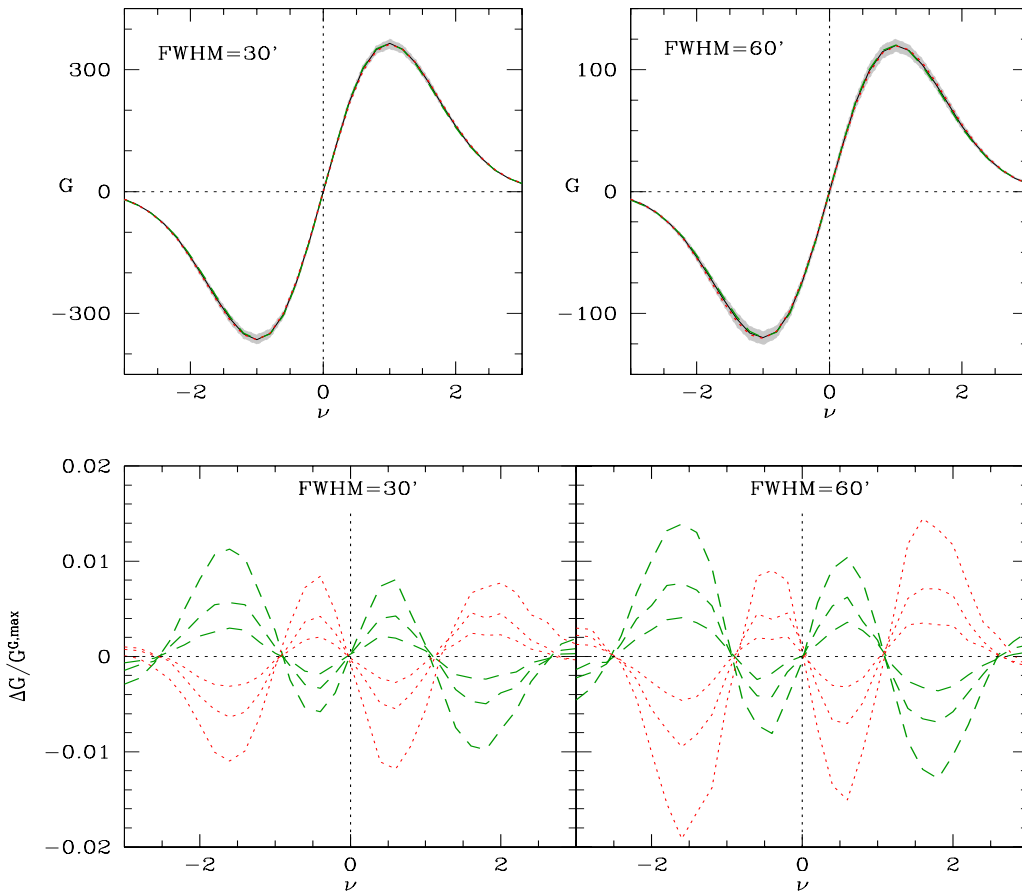


**Figure 4.** Variation of  $g(\nu)$  with  $g_{\text{NL}}$  for different smoothing angles. Results have been averaged over 200 realizations.  $G^{G,\text{max}}$  is the amplitude of the Gaussian genus evaluated at  $\nu = 1$ . Black (solid) lines are Gaussian, green (dashed) lines correspond to positive  $g_{\text{NL}}$  and red (dotted) to negative  $g_{\text{NL}}$ . The values of  $g_{\text{NL}}$  are  $\pm 5 \times 10^5$ ,  $\pm 1 \times 10^6$  and  $\pm 2 \times 10^6$ . The shaded regions in the top panels show the  $1\text{-}\sigma$  error bars for the Gaussian genus curve.

threshold temperature, denoted by  $\nu \equiv \Delta T / \sigma_0$ , where  $\sigma_0$  is the standard deviation of the temperature fluctuation. It is sensitive to the Gaussian/non-Gaussian nature of the fluctuation field and the shape of the underlying angular power spectrum. This makes it a useful tool to test non-Gaussianity. It was introduced in the context of the CMB in the seminal papers [46, 47]. It has been used extensively to study non-Gaussianity in a number of papers [48, 49, 50]. The genus is one of the three Minkowski functionals (MF's) [47, 51, 52], which are topological quantities that can be defined for a two dimensional field and which completely characterize its topological properties. The other two are the total iso-temperature contour length and the fraction of total area above the threshold. They have been used to constrain the  $f_{\text{NL}}$  parameter [43, 53, 54, 55].

For a given temperature threshold the genus is given by

$$G(\nu) = \frac{1}{2\pi} \int_C \kappa ds, \quad (19)$$

where  $\kappa$  is the signed curvature of the iso-temperature contours  $C$ . The genus can also be parametrized by the area fraction above the threshold. Using the temperature threshold is computationally easier, while the area fraction decreases correlations between the MF's [56]. Here we use the temperature threshold since we are focussing on the genus only.

For a given  $C_\ell$  and Gaussian smoothing angle  $\theta_s$ , related to FWHM as  $\theta_s = \text{FWHM}/2\sqrt{2\ln 2}$ , the genus per steradian of a Gaussian temperature field can be expressed as

$$G(\nu) = \frac{1}{2(2\pi)^{3/2}} \frac{\sum \ell(\ell+1)(2\ell+1)C_\ell F_\ell^2}{\sum (2\ell+1)C_\ell F_\ell^2} \nu e^{-\nu^2/2}, \quad (20)$$

where  $F_\ell$  is the smoothing filter, which for a Gaussian filter is given by  $F_\ell = \exp(-\ell(\ell+1)\theta_s^2/2)$ . For a weakly non-Gaussian field characterized by  $f_{\text{NL}}$ , approximate analytic expressions for the Minkowski functionals were obtained in [57, 58]. The expressions upto  $g_{\text{NL}}$  order on the perturbations have not been calculated yet. Here we study the topology of the temperature fluctuations that arise purely from  $g_{\text{NL}}$  non-Gaussianity by measuring the genus. For the computation of the genus we follow the method of [47]. We have used 31 threshold levels in the range -3 to 3. The amplitude and shape of the genus curve is sensitive to the smoothing scale and we have chosen three scales, FWHM = 30', 45' and 60' to demonstrate our results. Results become more noisy at higher smoothing scales since the number of structures (hot and cold spots) decrease. We have averaged the results over 200 maps for each value of  $g_{\text{NL}}$ .

Let us denote:

$$\Delta G(\nu) \equiv G^{\text{NG}}(\nu) - G^{\text{G}}(\nu), \quad (21)$$

where  $G^{\text{G}}(\nu)$  is the Gaussian genus and  $G^{\text{NG}}(\nu)$  is the non-Gaussian one. In Fig. (4) we have plotted  $G$  and  $\Delta G/G^{G,\text{max}}$ , where  $G^{G,\text{max}}$  is the amplitude of the Gaussian genus at  $\nu = 1$ . We have shaded the region within 1- $\sigma$  error bars for the Gaussian genus curves in the upper panels. It shows that for positive  $g_{\text{NL}}$ , the amplitude of the non-Gaussian genus curve is higher than the Gaussian one in the threshold range  $0 \lesssim |\nu| \lesssim 1$ , while it is lower in the range  $1 \lesssim |\nu| \lesssim 2.5$ . The fact that the genus is smaller in the range  $1 \lesssim |\nu| \lesssim 2.5$  means there are fewer hot spots and cold spots in the CMB map when non-Gaussian contribution with positive  $g_{\text{NL}}$  is present. Because of the larger genus amplitude at  $0 \lesssim |\nu| \lesssim 1$ , the range of  $\nu$  showing the sponge-like topology [59] (actually a two dimensional cut through sponge in the context of CMB) is smaller relative to the Gaussian one. When  $g_{\text{NL}}$  is negative, there are more hot as well as cold spots. Other than an overall scaling of the amplitude of  $\Delta G$ , the smoothing scale does not seem to affect its shape in the threshold range  $1 \lesssim |\nu| \lesssim 2.5$ .

In order to quantify the functional dependence of  $\Delta G/G^{G,\text{max}}$  we take the average of the magnitudes of its peak values (which lie roughly in the ranges  $1.5 < \nu < 2$  and

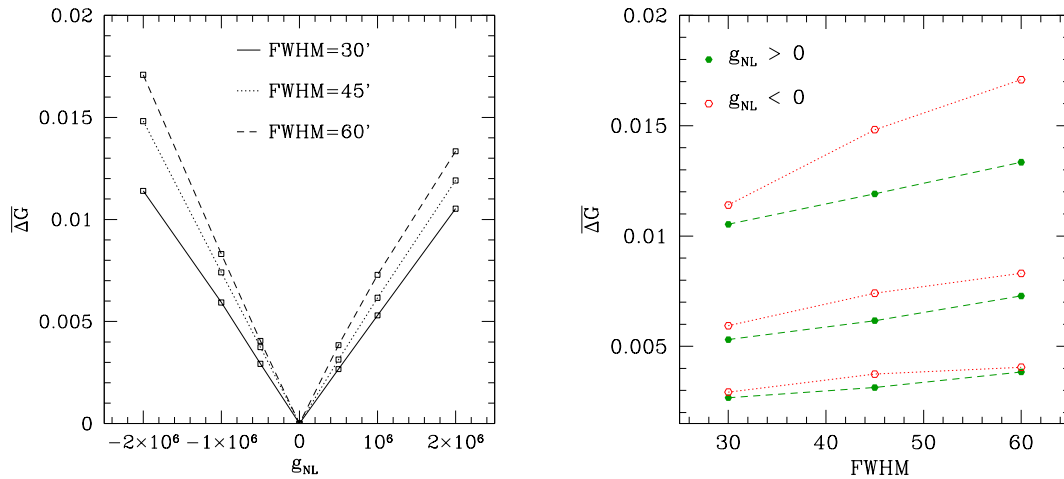


**Figure 5.** Functional dependence of  $\Delta G/G^{G,\text{max}}$  on  $g_{\text{NL}}$  and smoothing scale. In the right hand figure, the lines from the bottom to the top correspond to  $g_{\text{NL}} = \pm 5 \times 10^5, \pm 10^6, \pm 2 \times 10^6$ .

$-2 < \nu < -1.5$ ). Let us denote it by  $\overline{\Delta G}$ . In the left panel of Fig. (5) we have plotted the variation of  $\overline{\Delta G}$  with  $g_{\text{NL}}$  for FWHM 30', 45' and 60'. We find a linear dependence on  $g_{\text{NL}}$ , indicating that the leading order contribution to the deviation from the Gaussian genus curve comes from terms of order  $g_{\text{NL}}$ . The right panel shows the variation of  $\overline{\Delta G}$  with the smoothing scale for fixed  $g_{\text{NL}}$ . We find a mild increase as we increase FWHM, in the range of smoothing scales that we have studied.

So far we have described the number of structures for threshold range  $|\nu| < 2.5$ . Upto the smoothing scale of FWHM= 60' the number of structures above this threshold are not significantly large. However, an interesting observation that we have made for smoothing scales above FWHM= 60' is that the relative number of structures in this hottest or coldest range of threshold values,  $|\nu| > 2.5$ , compared to the range  $|\nu| < 2.5$ , grows significantly and hence promises to be useful for constraining  $g_{\text{NL}}$  at higher smoothing scales. We have not shown the results since the plots are quite noisy but we will be exploring this region further in subsequent work.

### 3.1. Other statistics derived from the genus

The genus at different threshold values is strongly (anti)correlated. One may then think of deriving other observables using the information inherent in the genus curves so that the non-Gaussian information may be maximized, and which may distinguish between different kinds of non-Gaussianity. The simulated non-Gaussian maps may then be used to test the sensitivity of these observables. We mention here four such quantities, namely,  $R_{\text{cold}}$ ,  $R_{\text{hot}}$ ,  $R_{\text{spots}}$  and  $S_0$ , which are defined below. Then we explore how they deviate from the Gaussian expectations.

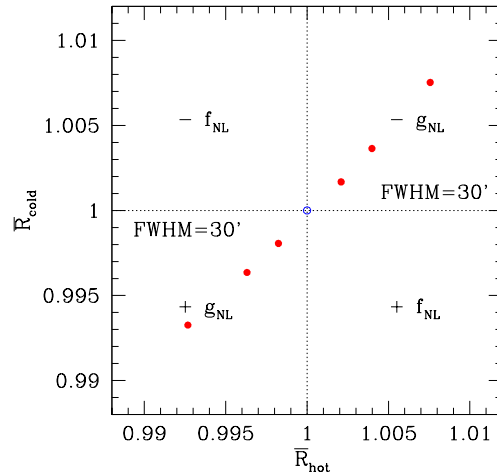


**Figure 6.**  $\bar{R}_{\text{hot}}$  vs.  $\bar{R}_{\text{cold}}$  for different values of  $g_{\text{NL}}$  for  $\text{FWHM} = 30'$ . The open circle at the center is the Gaussian mean while filled ones are  $g_{\text{NL}} = \pm 5 \times 10^5, \pm 1 \times 10^6$  and  $\pm 2 \times 10^6$ , at increasing distances from (1,1). The region where the mean values for positive and negative values of  $f_{\text{NL}}$  must lie, provided  $\text{FWHM} \lesssim 94'$ , are indicated. For  $\text{FWHM} \gtrsim 94'$ , they will interchange quadrants.

- (i)  $R_{\text{cold}}$ : Let  $N_{\text{cold}}$  denote the total number of cold spots, defined as  $N_{\text{cold}} \equiv \int_{-\nu_2}^{-\nu_1} d\nu G(\nu)$ , where  $\nu_1, \nu_2$  are suitably chosen positive threshold values with  $\nu_2 > \nu_1$ . Let  $G^{\text{fit}}(\nu)$  denote the Gaussian curve obtained by fitting the non-Gaussian genus points at different threshold values to a Gaussian shape. Let  $N_{\text{cold}}^{\text{G}} \equiv \int_{-\nu_2}^{-\nu_1} d\nu G^{\text{fit}}(\nu)$ . Then, we define

$$R_{\text{cold}} \equiv \frac{N_{\text{cold}}}{N_{\text{cold}}^{\text{G}}}. \quad (22)$$

For Gaussian maps, its value must be one. By inspecting Figs. (4) and choosing  $\nu_1 = 1$  and  $\nu_2 = 2.5$ , we can predict that for  $g_{\text{NL}} > 0$ ,  $N_{\text{cold}}$  must be less than one, whereas, for  $g_{\text{NL}} < 0$  it must be greater than one.

- (ii)  $R_{\text{hot}}$ : is defined to be the ratio  $N_{\text{hot}}/N_{\text{hot}}^{\text{G}}$ , where  $N_{\text{hot}}$  and  $N_{\text{hot}}^{\text{G}}$  are defined similar to  $N_{\text{cold}}$  and  $N_{\text{cold}}^{\text{G}}$ , but for integration in the positive threshold range. Again the Gaussian expectation is one, and for same  $\nu_1$  and  $\nu_2$  as above  $R_{\text{hot}} < 1$  for  $g_{\text{NL}} > 0$  and  $R_{\text{hot}} > 1$  for  $g_{\text{NL}} < 0$ . If  $\Delta G(\nu)$  is antisymmetric, as it appears to be in Fig. (4), then we must have  $R_{\text{hot}} = R_{\text{cold}}$ .
- (iii)  $R_{\text{spots}}$ : is defined to be the ratio  $N_{\text{spots}}/N_{\text{spots}}^{\text{G}}$ , where  $N_{\text{spots}} = N_{\text{cold}} + N_{\text{hot}}$  and  $N_{\text{spots}}^{\text{G}} = N_{\text{cold}}^{\text{G}} + N_{\text{hot}}^{\text{G}}$ . The Gaussian prediction of this statistic is one. For  $\nu_1 = 1$  and  $\nu_2 = 2.5$  it is less than one for  $g_{\text{NL}} > 0$  and greater than one for  $g_{\text{NL}} < 0$ .
- (iv)  $S_0$ : is defined as the ratio of the slope of the non-Gaussian genus curve and that of the fitted Gaussian at  $\nu = 0$ . It is greater than one for  $g_{\text{NL}} > 0$  and less than one for  $g_{\text{NL}} < 0$ .

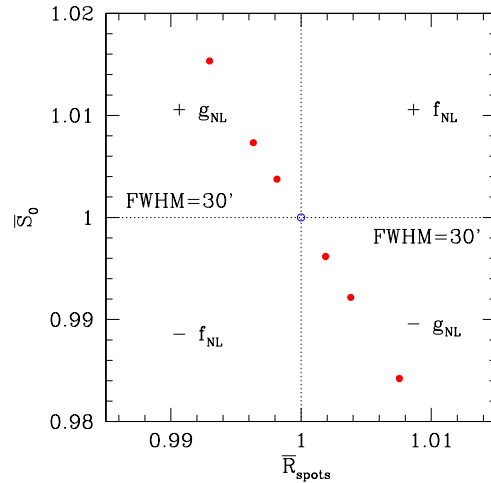


**Figure 7.**  $\bar{R}_{\text{spots}}$  vs.  $\bar{S}_0$  for different values of  $g_{\text{NL}}$  for  $\text{FWHM} = 30'$ . The open circle at the center is the Gaussian mean while the filled ones are  $g_{\text{NL}} = \pm 5 \times 10^5$ ,  $\pm 1 \times 10^6$  and  $\pm 2 \times 10^6$ , at increasing distances from (1,1). The region where the mean values for positive and negative values of  $f_{\text{NL}}$  must lie, provided  $\text{FWHM} \lesssim 94'$ , are indicated. For  $\text{FWHM} \gtrsim 94'$ , they will interchange quadrants.

In the case of non-Gaussianity arising from  $f_{\text{NL}}$ , since the shape of  $\Delta G$  is strongly dependent on the smoothing angle, these observables will depend on the smoothing angle. By judicious choice of  $\nu_1$  and  $\nu_2$  we can make them maximize the differences between  $f_{\text{NL}}$  and  $g_{\text{NL}}$  type non-Gaussianities. By inspecting Fig. (2) of Ref. [58] and choosing  $\nu_1 = 1$  and  $\nu_2 = 2.5$ , one can deduce that we must have  $R_{\text{cold}} < 1$ ,  $R_{\text{hot}} > 1$  for positive  $f_{\text{NL}}$  and  $R_{\text{cold}} > 1$ ,  $R_{\text{hot}} < 1$  for negative  $f_{\text{NL}}$ , when  $\text{FWHM} \lesssim 94'$ . The situation is reversed if  $\text{FWHM} \gtrsim 94'$ .  $S_0$  is always greater than one for positive  $f_{\text{NL}}$  and always less than one for negative case. For  $\text{FWHM} \lesssim 94'$ ,  $R_{\text{spots}} > 1$  if  $f_{\text{NL}} > 0$  and  $R_{\text{spots}} < 1$  if  $f_{\text{NL}} < 0$  and they interchange for  $\text{FWHM} \gtrsim 94'$ .

We next analyze the properties of these four observables inferred from the non-Gaussian maps. An overhead bar denotes the mean value of each of the above four statistics obtained by averaging over 200 realizations. Fig. (6) shows the parameter space  $(\bar{R}_{\text{hot}}, \bar{R}_{\text{cold}})$  for varying  $g_{\text{NL}}$  values, for  $\text{FWHM} = 30'$ . We have used  $\nu_1 = 1$  and  $\nu_2 = 2.5$  to calculate them. The open blue triangle at (1,1) indicates the Gaussian mean, while the red filled ones denote  $g_{\text{NL}} = \pm 5 \times 10^5$ ,  $\pm 1 \times 10^6$  and  $\pm 2 \times 10^6$ , at increasing distances from (1,1). In practice, the Gaussian mean has a small shift from (1,1) due to statistical fluctuation. We have corrected it by simply shifting it. We have then shifted the non-gaussian means by the same amount. This shift does not affect the relative distance between Gaussian and non-Gaussian means. Note that with minimal statistical fluctuation and if  $\Delta G$  is exactly anti-symmetric then the slope of the line  $(\bar{R}_{\text{hot}}, \bar{R}_{\text{cold}})$  will be exactly  $45^\circ$ .

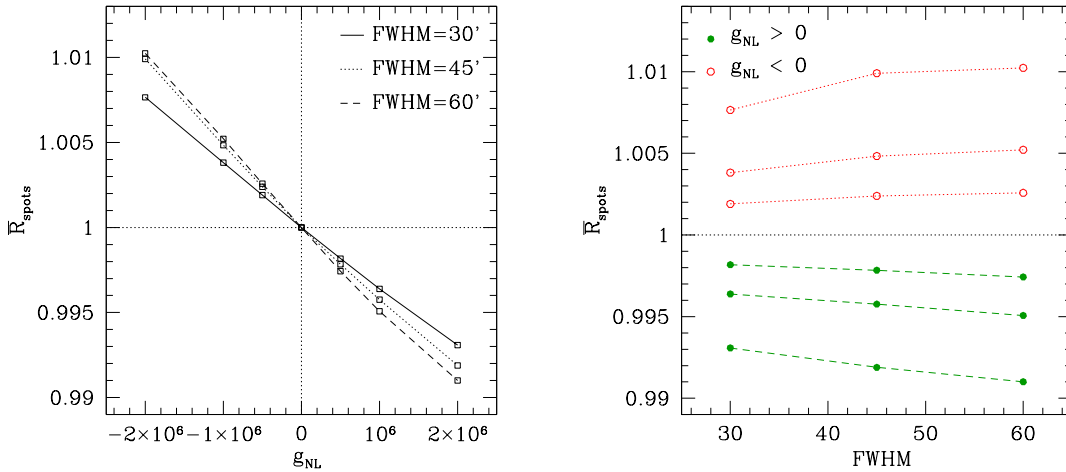


**Figure 8.** Functional dependence of  $R_{\text{spots}}$  on  $g_{\text{NL}}$  and smoothing scale. In the right hand figure, the lines get farther away from  $\overline{R}_{\text{spots}} = 1$  line as  $|g_{\text{NL}}|$  increases. The values are  $g_{\text{NL}} = \pm 5 \times 10^5, \pm 10^6, \pm 2 \times 10^6$ .

The parameter space  $(\overline{R}_{\text{hot}}, \overline{R}_{\text{cold}})$  gets divided into four regions, with negative  $g_{\text{NL}}$  occupying the first quadrant and positive  $g_{\text{NL}}$  the third, while  $\mp f_{\text{NL}}$  occupies the second and fourth quadrants, respectively. Larger smoothing angle increases the dispersion of the distribution of individual points  $(R_{\text{hot}}, R_{\text{cold}})$  about the mean because the number of structures decreases. But at the same time the size of deviations increases as smoothing scale increases, making the low resolution maps also useful in discriminating non-Gaussian maps from Gaussian ones.

Next we discuss the remaining two observables,  $\overline{R}_{\text{spots}}$  and  $\overline{S}_0$ . Fig. (7) shows the parameter space spanned by them for varying  $g_{\text{NL}}$ .  $\nu_1$  and  $\nu_2$  are the same as above. Again the blue triangle indicates the Gaussian mean, while the red ones denote  $g_{\text{NL}} = \pm 5 \times 10^5, \pm 1 \times 10^6$  and  $\pm 2 \times 10^6$ , at increasing distances from (1,1). The smoothing scale is  $\text{FWHM} = 30'$ , and the effect of smoothing scale is similar to above. The parameter space gets divided into four regions, with  $\pm g_{\text{NL}}$  occupying the second and fourth quadrants, respectively, while  $\pm f_{\text{NL}}$  occupies the first and third quadrants, respectively. Again for  $\text{FWHM} \gtrsim 94'$ , the positions of  $+f_{\text{NL}}$  and  $-f_{\text{NL}}$  will interchange.

Since  $R_{\text{spots}}$  carries information of both  $R_{\text{hot}}$  and  $R_{\text{cold}}$  we choose it for showing functional dependence of  $g_{\text{NL}}$  and FWHM. Panel 1 of Fig. (8) shows how  $R_{\text{spots}}$  varies with  $g_{\text{NL}}$  when FWHM is fixed. As is clear from the figure we find linear dependence, which agrees with the fact that we saw linear dependence of  $\overline{\Delta G}$  on  $g_{\text{NL}}$  in Fig. (5). Panel 2 of Fig. (8) shows functional dependence on FWHM for fixed  $g_{\text{NL}}$ . The lines get farther away from the Gaussian expectation,  $\overline{R}_{\text{spots}} = 1$ , as we increase  $|g_{\text{NL}}|$ . They exhibit mild increase with increase of the smoothing scale.

#### 4. Conclusion

We have simulated non-Gaussian CMB maps with the non-Gaussianity coming from purely third order perturbations of the primordial gravitational potential. We have used the map making algorithm proposed by [37] which computes  $a_{\ell m}$ 's as an integral in real space. This method is particularly advantageous for including the third order linearity, as compared to integrating in Fourier space since there are two  $k$  convolutions involved which make the computational very heavy.

We have investigated how the 1-point PDF gets modified from Gaussian shape due to the effect of the non-linearity parameter  $g_{\text{NL}}$ . We found that positive  $g_{\text{NL}}$  changes the 1-point PDF to leptokurtic shape and negative  $g_{\text{NL}}$  changes it to platykurtic shape. Its effect on the  $C_\ell$ 's is to increase power for large  $\ell$ 's for both positive and negative  $g_{\text{NL}}$  with the effect of negative  $g_{\text{NL}}$  being stronger.

We have next used the simulated maps to compute the genus curve and calculate their deviation from the Gaussian shape. The purpose is to understand their functional dependence on  $g_{\text{NL}}$  and how the non-Gaussian term modifies the topology of the CMB temperature field. We found that positive  $g_{\text{NL}}$  decreases both hot and cold spots in the threshold range  $1 \lesssim |\nu| \lesssim 2.5$  and increases the genus in the range  $0 \lesssim |\nu| \lesssim 1$ . The effect of negative  $g_{\text{NL}}$  is just the opposite. This results in antisymmetric shapes of  $\Delta G$ , which look approximately like sine functions. We do not find significant variation of the overall shape of  $\Delta G$  as we vary smoothing scale, but the amplitude of  $\Delta G$  decreases as we increase the smoothing scale. We found that the sensitivity of the negative and positive  $g_{\text{NL}}$ 's are roughly same. These results are very different from the genus arising from  $f_{\text{NL}}$ , which leads to symmetric form of  $\Delta G$  and which has strong dependence on the smoothing angle.

We have also studied four other statistics derived from the genus, namely, the number of hot spots, the number of cold spots, the combined number of hot and cold spots and the slope of the genus curve at  $\nu = 1$ . We found that these quantities carry distinct signatures of  $f_{\text{NL}}$  and  $g_{\text{NL}}$ . The parameter spaces get neatly divided into quadrants with each of the positive and negative  $g_{\text{NL}}$  and positive and negative  $f_{\text{NL}}$  occupying one. Hence they can be very useful for distinguishing these two different types of non-Gaussianities.

Since our goal was to get theoretical understanding of the nature of non-Gaussianity arising from  $g_{\text{NL}}$  term by means of studying statistical observables such as the genus and other quantities derived from it, we have not considered real observational contaminants such as point sources, instrument noise etc., to our simulations. One needs to take them into account for actual comparison with experimental data and putting constraints  $g_{\text{NL}}$ . Another interesting observable that we are studying using the non-Gaussian simulations is the correlation of peaks in the maps. These will be the subject of forthcoming publications.

## Acknowledgments

The authors acknowledge the support of the Korea Science and Engineering Foundation (KOSEF) through the Astrophysical Research Center for the Structure and Evolution of the Cosmos (ARCSEC). The computation in this paper was performed on the QUEST cluster at KIAS. P.C would like to thank Juhan Kim for his generous help while writing the codes, Qing-Guo Huang for many useful discussions and Michel Liguori for useful communication. We acknowledge use of the HEALPIX and CMBFAST packages.

## Appendix A. Simplified expressions for $W_\ell$

Here we present expressions which simplify the numerical computation of the filter function given in Eq. (17). Instead of doing the integral over product of two  $j_\ell$ 's, which is very time consuming due to the highly oscillatory behavior of  $j_\ell$ , we can simplify  $W_\ell$  to express it in terms of Gamma functions. Using  $j_\ell(kr) = \sqrt{\pi/2kr} J_{\ell+1/2}(kr)$  and  $P_\Phi(k) = A_0 \frac{k^{n_s}}{k^4}$  we get,

$$W_\ell(r, r_1) = \sqrt{\frac{A_0}{rr_1}} \int_0^\infty dk k^{-1/2} J_{\ell+1/2}(kr) J_{\ell+1/2}(kr_1) \quad (\text{A.1})$$

CASE 1 :  $r = r_1$ . Using the following formula [60],

$$\begin{aligned} \int_0^\infty dk k^{-\lambda} J_\nu(\alpha k) J_\mu(\alpha k) &= \frac{\alpha^{\lambda-1}}{2^\lambda} \frac{\Gamma(\lambda)}{\Gamma(\frac{-\nu+\mu+\lambda+1}{2})} \frac{\Gamma(\frac{\nu+\mu-\lambda+1}{2})}{\Gamma(\frac{\nu+\mu+\lambda+1}{2})} \\ &\times \frac{1}{\Gamma(\frac{\nu-\mu+\lambda+1}{2})}, \end{aligned} \quad (\text{A.2})$$

which holds when  $\nu + \mu + 1 > \lambda > 0$  and  $\alpha > 0$ , and putting  $\lambda = 1 - n_s/2$  we get,

$$W_\ell(r, r_1) = \frac{\sqrt{A}}{2^{1-\frac{n_s}{2}} r^{1+\frac{n_s}{2}}} \frac{1}{[\Gamma(1 - \frac{n_s}{4})]^2} \frac{\Gamma(1 - \frac{n_s}{2})}{\Gamma(\ell + \frac{1}{2} + \frac{n_s}{4})}. \quad (\text{A.3})$$

CASE 2:  $r \neq r_1$ . For this case, when  $\nu = \mu$ , we can use the following formula [60],

$$\begin{aligned} \int_0^\infty dk k^{-\lambda} J_\nu(\alpha k) J_\nu(\beta k) &= \frac{\alpha^\nu \beta^\nu}{2^\lambda (\alpha + \beta)^{2\nu-\lambda+1}} \frac{\Gamma(\nu + \frac{1-\lambda}{2})}{\Gamma(\nu + 1) \Gamma(\frac{1+\lambda}{2})} \\ &\times F\left(\nu + \frac{1-\lambda}{2}, \nu + 1/2, 2\nu + 1; \right. \\ &\quad \left. \frac{4\alpha\beta}{(\alpha + \beta)^2}\right) \end{aligned} \quad (\text{A.4})$$

which is holds provided  $2\nu + 1 > \lambda > -1$  and  $\alpha > 0$ ,  $\beta > 0$ .  $F(a, b; c; z)$  is the Gauss Hypergeometric function given by

$$F(a, b; c; z) = \frac{\Gamma(c)}{\Gamma(b)\Gamma(c-b)} \int_0^1 dt \frac{t^{b-1}(1-t)^{c-b-1}}{(1-tz)^a}, \quad (\text{A.5})$$

which is valid when  $c > b > 0$ . Then, using

$$\Gamma(2\ell) = \frac{1}{\sqrt{2\pi}} 2^{2\ell-1/2} \Gamma(\ell) \Gamma\left(\ell + \frac{1}{2}\right) \quad (\text{A.6})$$



and defining  $z$  as

$$z \equiv \frac{4rr_1}{(r+r_1)^2} = \frac{4r_1/r}{(1+r_1/r)^2}, \quad (\text{A.7})$$

we get

$$W_\ell(r, r_1) = \sqrt{\frac{A}{\pi}} 2^{n_s/2} \frac{z^\ell}{(r+r_1)^{1+n_s/2}} \frac{\Gamma(\ell + \frac{1}{2} + \frac{n_s}{4})}{\Gamma(1 - \frac{n_s}{4}) \Gamma(\ell + 1)} \\ \times \int_0^1 dt \frac{[(1-t)t]^\ell}{(1-tz)^{\ell + \frac{1}{2} + \frac{n_s}{4}}}. \quad (\text{A.8})$$

We can then scale the  $r$  dependence as,

$$W_\ell(r, r_1) = \frac{1}{r^{1+n_s/2}} \tilde{W}_\ell(r_1/r), \quad (\text{A.9})$$

where

$$\tilde{W}_\ell(r_1/r) = \sqrt{\frac{A}{\pi}} 2^{n_s/2} \frac{z^\ell}{(1+r_1/r)^{1+n_s/2}} \frac{\Gamma(\ell + \frac{1}{2} + \frac{n_s}{4})}{\Gamma(1 - \frac{n_s}{4}) \Gamma(\ell + 1)} \\ \int_0^1 dt \frac{[(1-t)t]^\ell}{(1-tz)^{\ell + \frac{1}{2} + \frac{n_s}{4}}}. \quad (\text{A.10})$$

Since  $r \neq r_1$  we have  $0 \leq z < 1$ . The integrand in Eq. (A.10) is a smooth positive function with a local maxima in the interval  $[0 : 1]$ . It becomes more and more localised as  $\ell$  increases and the peak position shifts towards one as  $z$  approaches one. The integral can be easily computed numerically.

## References

- [1] G. F. Smoot *et al.*, *Astrophys. J.* **396** L1 (1992).
- [2] A. H. Guth, *Phys. Rev. D* **23**, 347 (1981).
- [3] A. D. Linde, *Phys. Lett. B* **108**, 389 (1982).
- [4] A. J. Albrecht and P. J. Steinhardt, *Phys. Rev. Lett.* **48**, 1220 (1982).
- [5] T. Okamoto and W. Hu, *Phys. Rev. D* **66**, 063008 (2002) [arXiv:astro-ph/0206155].
- [6] N. Bartolo, E. Komatsu, S. Matarrese and A. Riotto, *Phys. Rept.* **402**, 103 (2004) [arXiv:astro-ph/0406398].
- [7] G. D'Amico, N. Bartolo, S. Matarrese and A. Riotto, *JCAP* **0801**, 005 (2008) [arXiv:0707.2894 [astro-ph]].
- [8] X. Chen, M. x. Huang and G. Shiu, *Phys. Rev. D* **74**, 121301 (2006) [arXiv:hep-th/0610235].
- [9] D. Seery, J. E. Lidsey and M. S. Sloth, *JCAP* **0701**, 027 (2007) [arXiv:astro-ph/0610210].
- [10] M. Li and Y. Wang, *JCAP* **0809**, 018 (2008) [arXiv:0807.3058 [hep-th]].
- [11] X. Chen, B. Hu, M. x. Huang, G. Shiu and Y. Wang, *JCAP* **0908**, 008 (2009) [arXiv:0905.3494 [astro-ph.CO]].
- [12] D. S. Salopek and J. R. Bond, *Phys. Rev. D* **42**, 3936 (1990).
- [13] T. Falk, R. Rangarajan and M. Srednicki, *Astrophys. J.* **403**, L1 (1993) [astro-ph/9208001].
- [14] V. Acquaviva, N. Bartolo, S. Matarrese and A. Riotto, *Nucl. Phys. B* **667**, 119 (2003) [arXiv:astro-ph/0209156].
- [15] J. M. Maldacena, *JHEP* **0305**, 013 (2003) [arXiv:astro-ph/0210603].
- [16] D. Seery and J. E. Lidsey, *JCAP* **0506**, 003 (2005) [arXiv:astro-ph/0503692].
- [17] K. M. Smith, L. Senatore and M. Zaldarriaga, arXiv:0901.2572 [astro-ph].
- [18] D. Seery and J. E. Lidsey, *JCAP* **0701**, 008 (2007) [arXiv:astro-ph/0611034].

- [19] K. T. Engel, K. S. M. Lee and M. B. Wise, *Phys. Rev. D* **79**, 103530 (2009) [arXiv:0811.3964 [hep-ph]].
- [20] A. D. Linde and V. F. Mukhanov, *Phys. Rev. D* **56**, 535 (1997)
- [21] D. H. Lyth and D. Wands, *Phys. Lett. B* **524**, 5 (2002)
- [22] M. Sasaki, J. Valiviita and D. Wands, *Phys. Rev. D* **74**, 103003 (2006)
- [23] C. T. Byrnes, M. Sasaki and D. Wands, *Phys. Rev. D* **74**, 123519 (2006).
- [24] K. Enqvist and T. Takahashi, *JCAP* **0809**, 012 (2008)
- [25] Q. G. Huang and Y. Wang, *JCAP* **0809**, 025 (2008)
- [26] P. Chingangbam and Q. G. Huang, *JCAP* **0904**, 031 (2009) [arXiv:0902.2619 [astro-ph.CO]].
- [27] Q. G. Huang, *JCAP* **0811**, 005 (2008) [arXiv:0808.1793 [hep-th]].
- [28] M. Sasaki, *Prog. Theor. Phys.* **120**, 159 (2008).
- [29] Q. G. Huang, *JCAP* **0905**, 005 (2009) [arXiv:0903.1542 [hep-th]].
- [30] Q. G. Huang, *JCAP* **0906**, 035 (2009) [arXiv:0904.2649 [hep-th]].
- [31] W. Hu, *Phys. Rev. D* **64**, 083005 (2001) [arXiv:astro-ph/0105117].
- [32] N. Kogo and E. Komatsu, *Phys. Rev. D* **73**, 083007 (2006) [arXiv:astro-ph/0602099].
- [33] G. De Troia et al., *Mon. Not. Roy. Astron. Soc.* **343**, 284 (2003) [astro-ph/0301294].
- [34] D. Jeong and E. Komatsu, arXiv:0904.0497.
- [35] V. Desjacques and U. Seljak, arXiv:0907.2257 [astro-ph.CO].
- [36] E. Komatsu, D. N. Spergel and B. D. Wandelt, *Astrophys. J.* **634**, 14 (2005) [arXiv:astro-ph/0305189].
- [37] M. Liguori, S. Matarrese and L. Moscardini, *Astrophys. J.* **597**, 57 (2003) [arXiv:astro-ph/0306248].
- [38] C. R. Contaldi and J. Magueijo, *Phys. Rev. D* **63**, 103512 (2001) [arXiv:astro-ph/0101512].
- [39] G. Rocha, M. P. Hobson, S. Smith, P. Ferreira and A. Challinor, "Simulation of non-Gaussian CMB maps," *Mon. Not. Roy. Astron. Soc.* **357**, 1 (2005) [arXiv:astro-ph/0406136].
- [40] R. Vio, P. Andreani, L. Tenorio, W. Wamsteker, *Publ. Astron. Soc. Pac.* **114**, 1281 (2002) [astro-ph/0207311].
- [41] E. Martinez-Gonzalez, J. E. Gallegos, F. Argueso, L. Cayon and J. L. Sanz, *Mon. Not. Roy. Astron. Soc.* **336**, 22 (2002) [astro-ph/0111284].
- [42] U. Seljak and M. Zaldarriaga, *Astrophys. J.* **469**, 437 (1996) [arXiv:astro-ph/9603033].
- [43] E. Komatsu *et al.* [WMAP Collaboration], *Astrophys. J. Suppl.* **180**, 330 (2009) arXiv:0803.0547 [astro-ph].
- [44] M. Liguori, A. Yadav, F. K. Hansen, E. Komatsu, S. Matarrese and B. Wandelt, *Phys. Rev. D* **76**, 105016 (2007) [Erratum-ibid. *D* **77**, 029902 (2008)] [arXiv:0708.3786 [astro-ph]].
- [45] K. M. Gorski, E. Hivon, A. J. Banday, B. D. Wandelt, F. K. Hansen, M. Reinecke and M. Bartelman, *Astrophys. J.* **622**, 759 (2005) [arXiv:astro-ph/0409513].
- [46] P. Coles, *Mon. Not. Roy. Astron. Soc.* **234**, 509 (1988).
- [47] J. R. Gott, C. Park, R. Juzkiewicz, W. E. Bies, F. R. Bouchet and A. Stebbins, *Astrophys. J.* **352**, 1 (1990).
- [48] C. Park, W. N. Colley, J. R. Gott, B. Ratra, D. N. Spergel and N. Sugiyama, *Astrophys. J.* **506**, 473 (1998) [astro-ph/9711057].
- [49] W. N. Colley and J. R. I. Gott, *Mon. Not. Roy. Astron. Soc.* **344**, 686 (2003) [arXiv:astro-ph/0303020].
- [50] C.G. Park, *Mon. Not. Roy. Astron. Soc.* , **349** 313 (2004) [astro-ph/0307469].
- [51] J. Schmalzing and K. M. Gorski, *Mon. Not. Roy. Astron. Soc.* , **297**, 355 (1998) [astro-ph/9712185].
- [52] S. Winitzki and A. Kosowsky, *New Astron.* **3**, 75 (1998) [arXiv:astro-ph/9710164].
- [53] J. R. I. Gott, W. N. Colley, C. G. Park, C. Park and C. Mugnolo, *MNRA* **000**, 1 (2006) [arXiv:astro-ph/0610764].
- [54] C. Hikage, T. Matsubara, P. Coles, M. Liguori, F. K. Hansen and S. Matarrese, *Mon. Not. Roy. Astron. Soc.* **389**, 1439 (2008) [arXiv:0802.3677 [astro-ph]].
- [55] P. Natoli *et al.*, arXiv:0905.4301 [astro-ph.CO].

- [56] S. F. Shandarin, H. A. Feldman, Y. Xu and M. Tegmark, *Astrophys. J. Suppl.* **41**, 1 (2002).
- [57] T. Matsubara, *Astrophys. J.* **584**, 1 (2003).
- [58] C. Hikage, E. Komatsu and T. Matsubara, *Astrophys. J.* **653**, 11 (2006) [arXiv:astro-ph/0607284].
- [59] J. R. . Gott, M. Dickinson and A. L. Melott, *Astrophys. J.* **306** (1986) 341.
- [60] I. S. Gradshtein and I. M. Ryzhik, *Table of Integrals*, 6th Edition, Academic Press (2000).